Radiation Monitor Extension for CMOS Imaging Instruments in Nanosatellites

Josua Florczak[1], Tom Neubert[1], Khalid El Maghawry[1], Egon Zimmermann[1], Heinz Rongen[1], Martin Kaufmann[2], Friedhelm Olschewski[3], Stefan van Waasen[1,4]

***Abstract*— With a software-based approach using commercial off-the-shelf CMOS imaging sensors to detect ionizing particles a low-cost radiation monitor is published to improve fault tolerance of nanosatellites with commodity hardware. We achieve this by segmenting image artefacts caused by radiation effects simultaneously within the original capturing images. For this purpose, a two-step segmentation method was developed using already acquired images from a miniaturized limb sounding spectrometer that derives atmospheric temperature profiles. The method covers badpixel elimination and particle flux determination by a minimalized amount of additional computational costs. This allows the determination of the radiation environment close to the imaging instruments inside the satellite. We present the segmented results and compare it with simulated as well as measured data from a reference radiation monitor experiment. The detected particle flux is up to a factor of five lower than the simulated flux. These effective particle flux values will be used to improve measurement time by triggering mitigation measures on demand and expand their life time.**

Index Terms— **CMOS, cosmic ray, CubeSat, dynamic threshold, low-cost, mitigation, radiation monitoring**

I. Introduction

Nanosatellites have evolved over the past 20 years and are no longer just demonstration platforms; they are also used for scientific applications. Remote sensing instruments as part of observation units are typically launched in low earth orbits (LEO) to provide global coverage [1],[2]. Realized with large pixel arrays, imaging capabilities are combined with spectrometer techniques e.g., to measure structures and temperatures with high spatial resolution. In order to meet these and other growing demands, current remote sensing applications [3] use scientific complementary metal oxide semiconductor (sCMOS) image sensors characterized by high signal-to-noise ratios, highly integrated readout electronics and low-cost procurement [4].

Longer mission durations are increasingly targeted for remote sensing instruments, e.g., to observe long-term climate processes. The mission lifetime will be influenced by radiation effects in electronic components. These radiation effects can be divided into cumulative effects (Total Ionizing Dose-TID and displacement damages) and single event effects (SEEs). While the cumulative effects lead to progressive degradation of components, SEEs cause problems such as bit flips, functional interruptions, or even destruction of components [5],[6]. Depending on the orbit, there are different radiation environments with low radiation dose rates in equatorial and higher in polar LEOs. The polar orbits require careful radiation protection and safety margins in design requirements, e.g. if the South Atlantic Anomaly (SAA) is passed [7]. To simplify design strategies, the use of particle detection can help respond to unexpected events such as geomagnetic storms, inhomogeneous or anisotropic radiation environments. Combined with on-demand mitigation measures, this can increase the use of standard scenarios in simulating the radiation environment, rather than worst-case scenarios. For example, no additional margin in shielding is required, resulting in savings in design costs and testing steps. In addition, mitigation techniques such as triggering protection circuits during heavy radiation fluxes may be feasible [7].

Customized CMOS image sensors or Monolithic Active Pixel Sensors (MAPS) have been used as particle detectors in space [10],[11], following developments at current particle accelerators like CERN [8],[9]. In addition, studies for particle detection with commercial of the shelf (COTS) based imaging sensors were initiated [12]. However, such additional particle detectors are not suitable for nanosatellites due to their additional mass, size, power consumption and cost.

In this paper, we extend the functionality of a COTS CMOS imaging sensor to include the ability to detect particles sufficiently well parallel to its original measurement task to determine the real radiation environment behind the shielding. As part of the AtmoSHINE instrument, the sensor is located in an imaging spatial heterodyne interferometer (SHI) launched in December 2018 to derive atmospheric temperature profiles. We use an adapted dynamic threshold method to determine the radiation environment. This low cost radiation monitor solution provides an extension to every imaging instrument and reacts against unexpected events and enables additional mitigation techniques on the satellite electronics. The methodological challenge in this integrated solution approach is to distinguish between the original measurement data and the radiation artifacts. Due to fast changing measurement scenes in single

[1] Central Institute of Engineering, Electronics and Analytics - Electronic Systems (ZEA-2), Forschungszentrum Jülich, Germany
[2] Institute of Energy and Climate Research (IEK-7), Forschungszentrum Jülich, Germany
[3] Institute for Atmospheric and Environmental Research, University of Wuppertal, Germany
[4] Faculty of Engineering, Communication Systems (NTS), University of Duisburg-Essen, Germany

pixel rows caused by variations of the position control system and varying stray light as well as the degradation effects of the sensor itself, single frame methods were needed.

The paper is structured as follows. First, we describe the measuring instrument that serves as a reference for our measurement and verification data, as well as the development of a method to flag and separate certain image artifacts. Afterwards, the quality is verified with a reference particle counter and simulated data. The accuracy and computational costs are analyzed and discussed in comparison to other cosmic ray segmentation methods. Finally, the first results of particle detection on real measured data are presented and potential protection measures are discussed. In the outlook, further development steps are outlined and additional planned functions of this monitor described.

II. Design Materials and Methods

A. Instrument overview

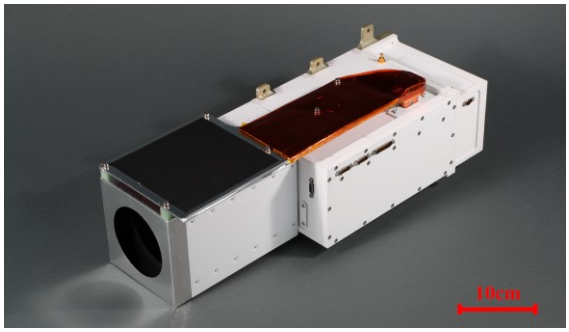

Fig. 1. AtmoSHINE flight model, a miniaturized Spatial Heterodyne Interferometer (SHI) launched as secondary payload in December 2018.

A highly miniaturized limb sounder (AtmoSHINE) suited for nano/micro satellites developed at Forschungszentrum Jülich utilizes a monolithic SHI for atmospheric temperature measurements [3] with a planned lifetime of 3 years [13]. It is a fully integrated remote sensing instrument with optics, focal plane array, electronics and shielded case, which is depicted in Fig. 1. The instrument operates as a secondary payload on a Chinese technology demonstration satellite. It is mounted on the shadow side of the satellite and measures the nighttime atmosphere from a sun synchronous orbit (SSO) at 1067 km altitude. To achieve the science mission objectives, selective hardening using state-of-the-art COTS components were used in combination with targeted mitigation measures.

The instrument contains a sCMOS sensor (HWK1910A) from Fairschield (BAE Systems) with a dimension of 5.04 µm x 5.04 µm and a total resolution of 1160 x 1976 pixels, which is well suitable for LEO operations [14]. The sensor is located close to the readout electronics and placed perpendicular to the viewing direction of the instrument.

AtmoSHINE has measured over a 10-month period since December 2018 in a timeshare with other instruments. During the observation periods, the instrument passes up to 14 times per day the SAA region. Fig. 2 (a) shows a typical undisturbed image of the spectral measurement and Fig. 2 (b) a disturbed one affected by radiation inside the SAA region. Both images show 2D-interferograms of the O2-A band night glow layer with spectral information in horizontal direction and spatial information in the vertical direction. Every image contains sensor specific artifacts e.g. bad pixel, and can be affected by anomalies caused by ionizing particles depicted in Fig. 2 (b).

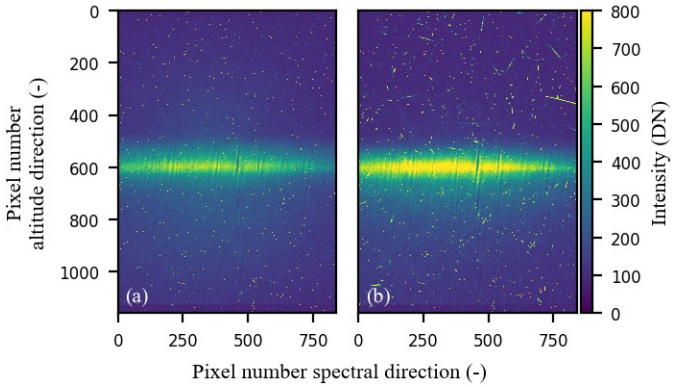

Fig. 2. (a) Undisturbed and (b) disturbed interferogram of the O2-A band nighttime limb emission by ionizing radiation as measured by the AtmoSHINE instrument. The left subfigure depicts measurements outside and right one inside the SAA.

B. Artefact Segmentation

Imaging artifacts are frequently observed in imaging sensors on satellites and interfere with the measurement data. In this work, artifacts are detected and segmented from measurement information and divided into sensor-specific and radiation-specific artifacts. A two-step approach based on an adapted dynamic threshold (ADT) is used to segment and separate these both artifact types. The two steps differ in the frequency of their execution and are marked as "on demand" and "frame by frame" in Fig. 3. For the first step, an adapted Interframe Statistics Median Filtering Detection (ISMFD) is implemented to segment the sensor-specific artefacts, such as more sensitive, dead or flickering single pixels, related to production processes and degradation effects [15]. This step requires multiple images and needs to be executed on demand, therefore this step can be done on the satellite in parallel as well as on ground. The second step involves segmented and separated radiation specific artefacts represented by variants of particle tracks, the number is counted and associated with an integral particle flux. This step has to be frame by frame. Both steps are designed to use a wide range of measurements so that they can be performed in parallel with the actual measurement in as many scenarios as possible.

1) Sensor artefacts

In this section, we take a closer look at the "Sensor-specific segmentation" task from the first on-demand step, which can be seen schematically in Fig. 3. To detect sensor-specific artifacts, we use a slightly modified form of the "Interframe Statistics Median Filtering Detection" (ISMFD) method [15]. The ISMFD performs flickering pixel detection in a measurement scene by using different single frames. Compared to other methods for detecting bad pixels [16], it uses simple arithmetic operations and is easily adaptable. Within the ISMFD, single thresholds r_{th} are still strongly dependent on the exposure level

of the measuring scene, which makes the processing more complex.

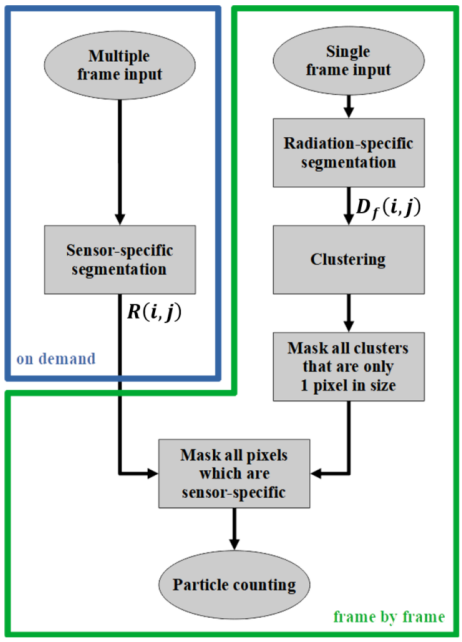

Fig. 3 Two-step segmentation flowchart. The 1st step (blue) segments sensor specific artifacts, which only needs to be performed from time to time either on the satellite or ground. The 2nd step (green) shows the segmentation of the detection, filtering and clustering radiation artefacts, which runs frame-by-frame in parallel to the actual measurements.

In order to make the segmentation more independent according to different exposure levels, we introduce an advanced method based on a relative gain matrix

$$r_f(i,j) = g_f(i,j)/\widetilde{m_f}(i,j) \ , \tag{1}$$

where $g_f(i,j)$ is an original image *f*, as shown in Fig. 2, and $\widetilde{m_f}(i,j)$ is the median image containing the median intensity by the direct neighbors. The lines and columns are identified with *i* and *j*. The relative gain with a homogeneous exposure is ideally 1 and independent of the exposure level. Here we assume that the immediate neighboring pixels of a currently viewed pixel at position *i*, *j* represent a relatively homogeneous exposure scene. Because of an overall non-homogeneous exposure, we have chosen a relatively small median filter window of only 3x3 pixels in order to calculate the median image. The adaptation in Eq. (1) makes the approach simpler, usable for night and daylight measurements and can be used more generally and offers to set a threshold r_{th} after a one-time analysis instead of determining this threshold every time.

A single frame bad pixel matrix

$$N_f(i,j) = \begin{cases} 1 \text{ if } r_f(i,j) > r_{th} \\ 0 \text{ else} \end{cases} \text{ with } \ r_{th} = 1 + \alpha \times \sigma \ , \tag{2}$$

can now be calculated depending on the threshold value r_{th} and the gain matrix where the threshold value r_{th} is calculated from standard deviation σ of multiple relative gain matrices $r_f(i,j)$. In the analyzed histograms of the relative gain of the images, a normal distribution is expected with a mean of 1 and a standard deviation depending on the manufacturing process and the degradation of the sensor. The selection of α depends on the pixel quality of the detector and the requirements for a non-bad pixel, which we iterate to a value of 3.

To consider time variant artefacts, e.g. flickering pixels and not only permanent bad pixels, analysis of multiple frames is necessary. Here we chose the detection of flickering bad pixels according to the ISMFD. Using a probability threshold $k_{r_{th}}$ for the flickering of bad pixels and by means of multiple single analyzed bad pixel maps $N_f(i,j)$, we can calculate a final bad pixel matrix

$$R(i,j) = \begin{cases} 1 \text{ if } \sum_{f=1}^{Q} N_f(i,j) \geq k_{r_{th}} \\ 0 \text{ else} \end{cases} \tag{3}$$

where Q is the total number of frames acquired in a short contiguous time period. From the pre-analyzed histogram of relative gains, we know how many bad pixels we expect after Q frames. Therefore, the value $k_{r_{th}}$ is set to a value by which the number of permanent bad pixels $\sum_{i,j} R(i,j)$ equals to the average number of bad pixels per frame expected from the histogram $\frac{\sum_{f,i,j} N_f(i,j)}{Q}$.

With the resulting total matrix of bad pixels $R(i,j)$, the quality of the segmentation can be improved in a second step by detecting false positive radiation-specific artifacts. Since the number of bad pixels increases with the TID, the bad pixel determination should be repeated after a certain radiation dose or time period.

2) *Radiation artefacts*

Radiation-specific artifacts are pixels affected by ionizing particles. Artifacts are clustered into particle tracks and blobs. The intensity and shape of these particle tracks depend on the particle type, its energy, and the angle of impact on the sensor surface [11]. For detection of these artifacts in single-shot exposure imaging, common frame-based algorithms exist, e.g. Detect and Remove Cosmic Rays (DCR, [17]) and Laplacian cosmic-ray rejection (L.A. Cosmic, [18]) [19].

Here, an Adapted Dynamic Threshold (ADT) method was used considering nanosatellites criteria of limited processing and memory capacities. ADT is a simple method with a small parameter space and sufficient shape preservation of particle tracks. The algorithm considers an approach which is similar to Kirsch's method [20]. Kirsch set a fixed value of 25% to estimate the background, the method was tested against images of dark background only.

In ADT, a percentile value $P_n^i(g_f)$ is applied for our application row-wise perpendicular to interferogram lines for each frame *f*, due to the spatial information of the dataset. The *n*-th percentile is an estimation of the image background at row i. $P_n^i(g_f)$ is multiplied by parameter β to set the threshold for each row. Unlike [20], parameter β is introduced to decrease the false positive detected pixels. The range of β is estimated based on the dynamical range of the sensor.

$$D_f(i,j) = \begin{cases} 1, if\ g_f(i,j) > \beta * P_n^i(g_f(i,j)) \\ 0, else \end{cases}, \quad (4)$$

where $\beta * P_n^i\left(g_f(i,j)\right)$ is less than the total number of quantization steps, g_f is the input frame and D_f is the obtained boolean matrix of detected radiation-specific artifacts pixels for each frame (f).

Finally, as shown in Fig. 3, the detected pixels are clustered with their direct neighboring pixels to identify the particle tracks. All clusters with a size of only 1 Pixel are eliminated, because they are either undetected sensor artefacts or only weak interacting electrons [30]. The sensor-specific artifacts are eliminated by applying the bad pixel matrix $R(i,j)$ obtained by equation (3). The clustered artifacts enables us to count the particle tracks and to obtain the integral particle flux.

Parameters $P_n^i(g_f)$ and β are optimized by tuning both of them based on the algorithm performance properties explained in section II.C.

C. Validation of segmentation and quantification

1) Algorithm Validation

In order to verify the ADT algorithm, referenced data is chosen from an in-orbit Space Application of Timepix Radiation Monitor (SATRAM) [11]. SATRAM provides data in similar spatial and temporal context as AtmoSHINE and utilizing an AtmoSHINE-like sensor technology. Various dark images with particle tracks and blobs from SATRAM open access database [21] are merged with undisturbed interferogram image from AtmoSHINE instrument. Pixel values of SATRAM are scaled to the range of interferogram image pixel values to obtain a data set of CMOS images with predetermined artifacts referred in this paper as merged data. We picked a data set of images of filling factor ranges from <1% to 58% representing different radiation conditions. Filling factor is defined by the percentage of image pixels that are disturbed by charged particles [19]. Such a data set enabled us to evaluate the algorithm effectively and compare it to L.A. Cosmic and DCR algorithms.

We evaluated ADT algorithm performance using the merged data and compared it to the performance of L.A. Cosmic and DCR algorithms. L.A. Cosmic uses a convolution Laplacian edge detection method [18] while DCR analyzes histograms of small-sized sub-frames to find deviations from the Gaussian distributions made by artifacts pixels [17]. The performance was evaluated in terms of three quantified properties: detection efficiency of pixels (E_{pix}), false-positive F_{+ve} and the counts of clusters (N_c) [19]. Detection efficiency is the fraction of true positive detected artifacts out of the total predetermined artifacts, while false positive is the percentage of pixels falsely detected as artifacts relative to the number of undisturbed pixels. The counts of clusters are expressed in percentage as how many clusters of SATRAM were segmented successfully.

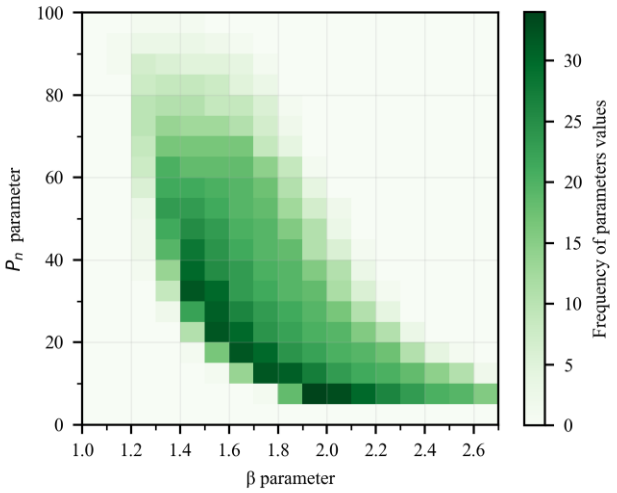

Fig. 4 Parameter optimization plot. The values of the axes show the optimization parameters and the frequency (z-axis), that meets the performance properties constraints. The maximum value describes the optimized algorithm parameter setting.

The three properties were essential for optimizing ADT, L.A. Cosmic and DCR algorithms. We set boundary conditions for E_{pix}, F_{+ve} and N_c and investigated how often they were achieved with different parameter settings for images with different levels of disturbance. The plot in Fig. 4 shows the frequency of parameter $P_n^i(g)$ and β values that meet performance properties constraints $E_{pix} > 95\%$, $F_{+ve} < 0.5\%$ and N_c is in the range of $\pm 10\%$. The optimum values of $P_n^i(g)$ is 5-10% at β values range from 1.9-2.0 for the filling factor range 1-58%. Other algorithms such as L.A. Cosmic and DCR were optimized in the same way with different constraints to carry out performance comparisons discussed in section III.A.

2) Radiation Environment Simulation

Beside the segmentation efficiency evaluation, the integral particle flux as result of the artefact segmentation was compared to pre-mission simulations that were also used in previous designs [13]. The integral ionizing radiation flux is determined by a flux of galactic cosmic rays (GCR), solar particles, and trapped particles, each simulated with simulation models provided in tools like SPENVIS [22] or OMERE [23]. With these tools the effective shielding of the instrument was also examined and determined.

With SPENVIS we simulated the AtmoSHINE environment on a SSO with 1067km altitude and an inclination of LTAN 06:30 UTC. The simulated flux of trapped protons and electrons is based on AP8 and AE8 [[24]-[26]] model, solar particles with Xapsos [27] and galactic cosmic rays with ISO-15390 model. With the "Short-term Single Event Upsets" section in SPENVIS we account the effective shielding of the satellite. The integral particle flux is calculated, based on MFLUX module provided in SPENVIS for previously defined orbit points with a freely adjustable shielding thickness. This allows us to compare the simulated particle rates in the same grid to the satellite measurement points.

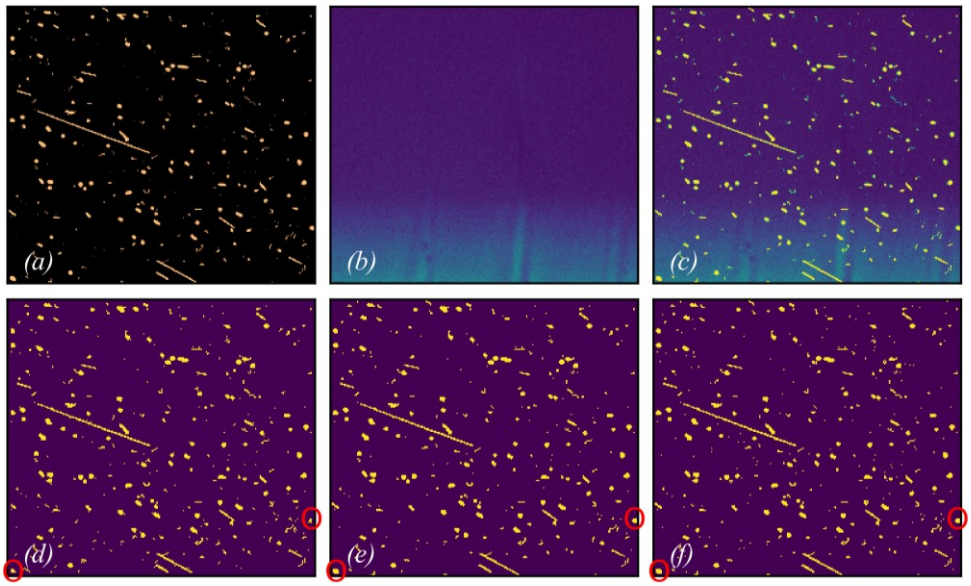

Fig. 5 Upper row: (a) SATRAM image, (b) sub-image of undisturbed AtmoSHINE frame and (c) the merged sub-image. Lower row: Boolean detection maps of (d) Laplacian Cosmic algorithm, (e) Adapted Dynamic Threshold method and (f) Detect and remove cosmic rays. Red circles point limited edge detection of L.A. Cosmic comparing to ADT and DCR.

III. Results

In order to check ADT algorithm performance and validate the results we used SATRAM data as mentioned in the section II.C and compared it to L.A. Cosmic and DCR. The comparison aspects are detection performance, counts of clusters, and computational complexity. The optimum performance is the one that matches the limited processing and memory capacities of nanosatellites. We then compare the particle flux rate calculated by the ADT using real measured data from AtmoSHINE with the expected simulated results from SPENVIS. In the end, we compare the effects of both particle flux rates on a selected mitigation method.

A. Detection performance

Using optimized parameters for each algorithm, they detected the particle tracks of the merged image Fig. 5 (c) as shown in Fig. 5 (d-f). The merged image was made of the original undisturbed AtmoSHINE image Fig. 5 (b) and the SATRAM reference image of ~4% filling factor Fig. 5 (a). By quick visual inspection, all algorithms show sufficient detection and artifacts shape preservation at filling factor 4% Fig. 5 (d-f).

For quantitative analysis, the performance properties: detection efficiency of pixels, false-positive number and counts of clusters are calculated for each algorithm as a function of filling factor Fig. 6 (a-c) respectively. In Fig. 6 (a), the three algorithms show good detection efficiencies at low filling factors till ~10% (weak conditions).

As it is getting harder to clearly separate pixel clusters from each other with more than 10 % of pixels disturbed [11]. DCR efficiency declines sharply at filling factors >10%. The sharp decline is due to the sub-frame histogram detection method used by the algorithm. The artifact pixels predominate the local distribution of pixels values. This predominance increases the threshold value for the sub-frame missing most of artifact pixels.

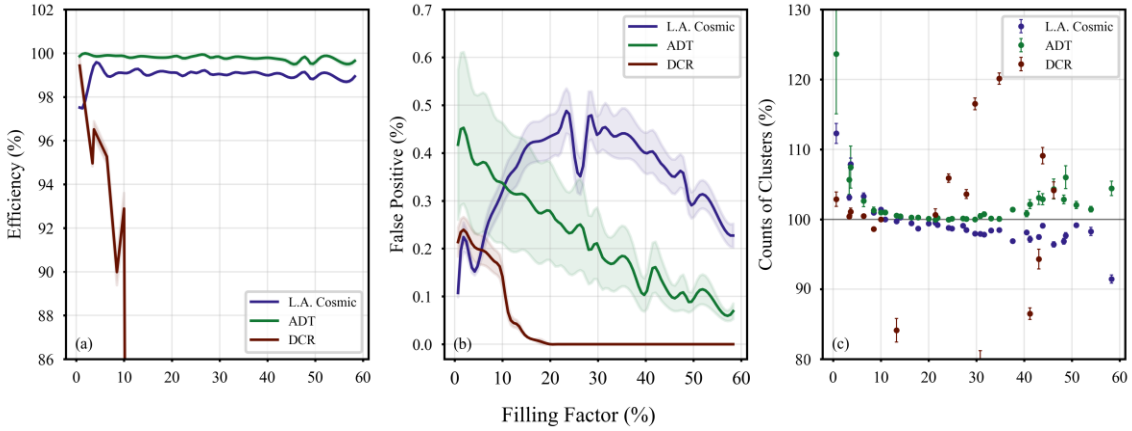

Fig. 6 Comparison of pixel detection efficiency (a), numbers of false positive detected pixels (b) and percentage of cluster deviation (c) for L.A Cosmic, Adapted dynamic threshold (ADT) and DCR. The DCR is not efficient for filling factors >10% as seen in (a), so the values for the DCR from (b-c) are not very conclusive. Because of the chosen parameters, the ADT is slightly over-sensitive in detection, results into higher numbers of false positive detected pixels (b) and the L.A. Cosmic shows a non-monotonic behavior. The deviation for small fill factors in (c) is caused by the small absolute number of detected clusters.

Although L.A. Cosmic misses the edges of the image during the convolution process as pointed in red circles in Fig. 5 (d), L.A. Cosmic shows efficiencies >98% similar to ADT for the same data set. The false positive numbers F_{+ve} of all three algorithm are highly dependent on the filling factor. ADT is decreasing and shows small numbers for higher filling factor Fig. 6 (b). It should be pointed out that in the same figure DCR indicates a decreasing number of false positive pixels with the filling factor, but this is only due to the decrease of the detection capability of the algorithm at fill factors >10%. In Fig. 6 (c) we see that the ADT for filling factors above 1% has an uncertainty <8% and basically tends to identify more clusters, the L.A. Cosmic of <10%, as well as basically identifies fewer clusters and the DCR scatters strongly at filling factors >10% .

The other aspect of the comparison analysis is the computational complexity to fit satellite's resources. Based on the used methods by each algorithm, we can define the O-notation for each of them to calculate the number of running operations. *Astroscrappy* [28] is the used python package in this study to run L.A. Cosmic. The package is convolving the image (MxN) with Laplacian kernel of size (kxk). The convolution process is $I(MxN) * (kxk)$ which implies to quadratic O-notation $O(n^2)$. DCR is well optimized in C language. The histogram has a quadratic notation [32] also run for the number of sub-frames N_{subf} . The O notation of DCR is $(N_{subf} n^2)$. On the other hand ADT uses an optimized *numpy* percentile function utilizing quick sorting function of quasi-linear complexity $O(nlog(n))$. A quantitative analysis of run time using a machine of six CPUs with 2.20GHz each and 16 GB RAM is carried out against the image size matches the previously mentioned complexities. The analysis of run time using the same machine is extended against the filing factors Fig. 7. As shown in Fig. 7 (c), DCR shows high dependency on the filling factor, run time increases till ~10%filling factor before decreasing sharply due to detection efficiency decline. L.A. Cosmic and ADT are more independent of filling factor Fig. 7 (a,b). The quasilinear O-notation of ADT gives the algorithm advantage of being computationally cheaper than L.A. Cosmic by one order of magnitude.

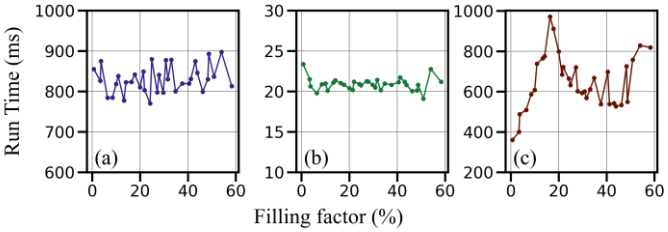

Fig. 7 Comparison of runtime for (a) L.A. Cosmic, (b) ADT and (c) DCR at different filling factors.

B. *Observed integral particle flux*

During observation on 7 August 2019, interferograms were acquired using a region of interest of 840x1160 pixels for day and nighttime with a total of 2072 measurements. Each acquired image of the AtmoSHINE instrument was analyzed by the ADT and bad pixels were removed. These images were acquired with the CMOS sensor inside the instrument, and the results imply the effective shielding of the satellite. The integral particle flux as result of the artifact segmentation is plotted in Fig. 8 (a) for the location of the satellite and varies about three orders of magnitude in this period, with the highest values when passing the SAA region.

Fig. 8 (b) shows the time distribution of integral particle flux according to the simulation with SPENVIS and the determined integral particle flux of the ADT by using the AtmoSHINE data. The corresponding regions are labeled and show a suitable correlation in the SAA region. The difference in particle fluxes by an order of magnitude can be explained by daily fluctuations [29], which differ significantly from the long-term averaged values used in simulation. In addition, we considered variances in effective shielding thickness of ± 4 mm. Such variances can occur with secondary payloads, but also with inhomogeneous radiation. Due to the effective shielding thicknesses in the current design, electrons are not dominant in the expected particle flux, which allows using the simulating models where electrons are only partially considered compared to the well-modeled protons [13]. In addition, the interaction of electrons with electronics is much weaker than for heavier ionizing particles, so electrons are negligible for further considerations [30].

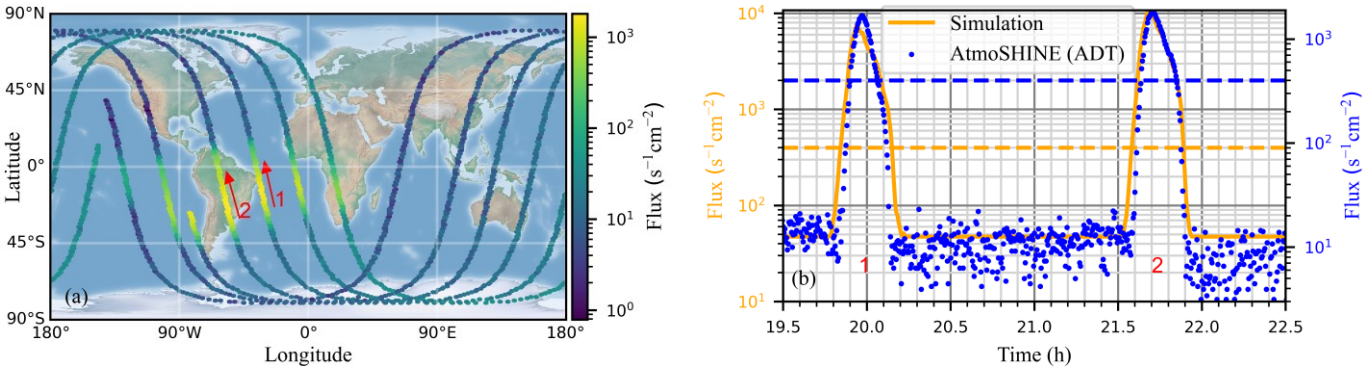

Fig. 8. (a) Spatial and (b) time distributions of integral particle flux calculated with the ADT by using the AtmoSHINE measurements on 7 August 2019 at an altitude of 1073km. The data shown in (b) provide a section of a 3-hour orbit with two tracks passing the SAA. Time distribution is compared with simulated integral particle flux including an equivalent Al shielding thickness of 6 mm. For orientation, the corresponding regions in (a) and (b) are marked in red and in (b) a threshold value for further mitigation measures is marked with two dashed lines.

C. Mitigation measures

As result of particle counting, additional mitigation measures can be identified. Once, real-time monitoring can be implemented to record the accumulated dose rates [31] and thus also detect degradation defects in the sensor or identify bad pixels. In addition, adjusted exposure times can improve data quality depending on the radiation environment. Furthermore, at a predefined particle flux threshold, it may be possible to protect the instrument by selectively switching sensitive components on and off. Investigations based on simulation data were performed by Neubert et al. [13] and results in a reduction of failure rate due to Single Event Upsets (SEUs) in the electronics by a factor of four. This measure is coupled with a limitation in measurement time.

For that case, in Fig. 9 the shutdown time per orbit is plotted against the integral particle flux threshold on the x-axis. As in Fig. 8 (b), an exemplary threshold value of 400 particles / (s cm^2) (red line) is plotted. Using this threshold and taking into account the deviations due to shielding, it results in up to 9 % less shutdown time to achieve a similar reliability of the instrument. This corresponds to an effective extension of the measurement time by approx. 2 hours per day. The difference between simulation and measurement remains relatively constant in the range of 60-2000 particles / (s cm^2).

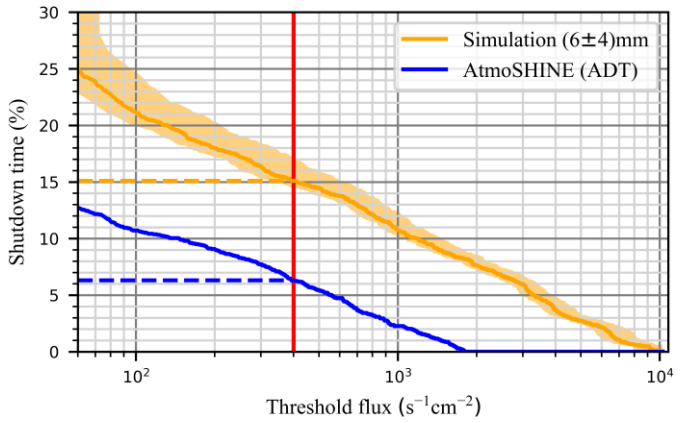

Fig. 9. Relative shutdown time for different threshold flux values on 7 August 2019. The difference in shutdown time between simulated (orange) and measured (blue) particle flux by short-term fluctuations is shown according for a given threshold line (red). Simulation results include an equivalent Al shielding thickness of 6mm and their margins.

IV. Conclusion

With measurement data of the AtmoSHINE instrument, the feasibility of a radiation monitor based on COTS sCMOS sensors could be demonstrated. A two-step approach is used to detect sensor- and radiation-specific artifacts, were an adapted dynamic threshold method drives the segmentation of the radiation-specific artifacts. It was shown that the ADT is one magnitude of order faster compared to other common segmentation methods and has a much smaller parameter space with only two parameters, which allowed a fast and easy optimization of the parameters. Using the ADT, on more than 99% of the pixels affected by ionizing particles were detected and only a few pixels were detected falsely positive. By clustering the segmented artifacts, the particle rate could be determined with an uncertainty of <8%.

In the future, the approach will enable real-time detection of sensor degradation effects, setting demand-controlled exposure times to improve data quality, or triggering additional mitigation measures. It was shown that the count rates per measurement point can be up to an order of magnitude lower compared to simulation results, which enable us to react directly to the effective radiation condition behind the shielding, e.g. by selectively switching off the instrument. This increases the lifetime and it has been shown that the measurement time can be extended up to 2 hours per day using the ADT compared to estimations based on simulation.

Further studies are planned to determine the effective energies of the particles and resulting LET spectra. This would allow a real-time analysis of the actual SEU error rates in order to operate the instrument with further mitigation measures even longer in orbit and to enable long-term observations.

References

[1] J. Bouwmeester and J. Guo, “Survey of worldwide pico- and nanosatellite missions, distributions and subsystem technology,” *Acta Astronautica*, vol. 67, no. 7–8, pp. 854–862, Oct. 2010, doi: 10.1016/j.actaastro.2010.06.004.

[2] A. Poghosyan and A. Golkar, “CubeSat evolution: Analyzing CubeSat capabilities for conducting science missions,” *Prog. in Aerosp. Sciences*, vol. 88, pp. 59–83, Jan. 2017, doi: 10.1016/j.paerosci.2016.11.002.

[3] M. Kaufmann *et al.*, “A highly miniaturized satellite payload based on a spatial heterodyne spectrometer for atmospheric temperature measurements in the mesosphere and lower thermosphere,” *Atmos. Meas. Tech.*, vol. 11, no. 7, pp. 3861–3870, Jul. 2018, doi: 10.5194/amt-11-3861-2018.

[4] R. Turchetta, “CMOS monolithic active pixel sensors (MAPS) for scientific applications: Some notes about radiation hardness,” *Nucl. Instrum. Methods Phys. Res. Sect. A: Accelerators, Spectrometers, Detectors and Associated Equip.*, vol. 583, no. 1, pp. 131–133, Dec. 2007, doi: 10.1016/j.nima.2007.08.226.

[5] K. A. LaBel *et al.*, “Commercial microelectronics technologies for applications in the satellite radiation environment,” in *1996 IEEE AeroConf. Proc.*, Aspen, CO, USA, Feb. 1996, vol. 1, pp. 375–390. doi: 10.1109/AERO.1996.495897.

[6] M. Campola. (2018, Jul.). Taking Smallsats to the Next Level - Sensible Radiation Requirements and Qualification That Won’t Break the Bank. *Proc. of the AIAA/USU Conf. on Small Satellites*. Utah, United States. [Online]. Available: https://digitalcommons.usu.edu/smallsat/2018/all2018/445/. Accessed: Nov. 04, 2019.

[7] D. Sinclair and J. Dyer. (2013, Aug.). Radiation Effects and COTS Parts in SmallSats. *Proc. of the AIAA/USU Conf. on Small Satellites*. Utah, United States. [Online]. Available: https://digitalcommons.usu.edu/smallsat/2013/all2013/69/. Accessed: Nov. 20, 2019.

[8] P. Yang *et al.*, “MAPS development for the ALICE ITS upgrade,” *J. Instrum.*, vol. 10, no. 03, pp. C03030–C03030, Mar. 2015, doi: 10.1088/1748-0221/10/03/C03030.

[9] W. Snoeys, “CMOS monolithic active pixel sensors for high energy physics,” *Nucl. Instrum. Methods Phys. Res. Sect. A: Accelerators, Spectrometers, Detectors and Associated Equip.*, vol. 765, pp. 167–171, Nov. 2014, doi: 10.1016/j.nima.2014.07.017.

[10] E. F. Mitchell *et al.*, “The Highly Miniaturised Radiation Monitor,” *J. Instrum.*, vol. 9, no. 07, pp. P07010–P07010, Jul. 2014, doi: 10.1088/1748-0221/9/07/p07010.

[11] C. Granja *et al.*, “The SATRAM Timepix spacecraft payload in open space on board the Proba-V satellite for wide range radiation

monitoring in LEO orbit," *Planet. and Space Sci.*, vol. 125, pp. 114–129, Jun. 2016, doi: 10.1016/j.pss.2016.03.009.

[12] M. Pérez *et al.*, "Particle detection and classification using commercial off the shelf CMOS image sensors," *Nucl. Instrum. Methods Phys. Res. Sect. A: Accelerators, Spectrometers, Detectors and Associated Equip.*, vol. 827, pp. 171–180, Aug. 2016, doi: 10.1016/j.nima.2016.04.072.

[13] T. Neubert *et al.*, "System-on-module-based long-life electronics for remote sensing imaging with CubeSats in low-earth-orbits," *J. Appl. Rem. Sens.*, vol. 13, no. 03, pp. 1–17, Jul. 2019, doi: 10.1117/1.JRS.13.032507.

[14] J. Liu *et al.*, "Investigation on a SmallSat CMOS image sensor for atmospheric temperature measurement," in *Int. Conf. on Space Opt. — ICSO 2018*, Chania, Greece, Jul. 2019, vol. 11180, pp. 2384–2393. doi: 10.1117/12.2536157.

[15] Yang Cao, Weiqi Jin, Chongliang Liu and Xiu Liu, "Scene-based bad pixel dynamic correction and evaluation for IRFPA device," in *Advances in Optoelectronics and Micro/nano-optics*, Guangzhou, China, Dec. 2010, pp. 1–4. doi: 10.1109/AOM.2010.5713516.

[16] W. Isoz, T. Svensson and I. Renhorn, "Nonuniformity correction of infrared focal plane arrays," in *Infrared Technol. and Applications XXXI*, Orlando, Florida, USA, May 2005, vol. 5783, pp. 949–960. doi: 10.1117/12.606691.

[17] W. Pych, "A Fast Algorithm for Cosmic-Ray Removal from Single Images," *PUBL ASTRON SOC PAC*, vol. 116, no. 816, pp. 148–153, Feb. 2004, doi: 10.1086/381786.

[18] P. G. van Dokkum, "Cosmic-Ray Rejection by Laplacian Edge Detection," *PUBL ASTRON SOC PAC*, vol. 113, no. 789, pp. 1420–1427, Nov. 2001, doi: 10.1086/323894.

[19] C. L. Farage and K. A. Pimbblet, "Evaluation of Cosmic Ray Rejection Algorithms on Single-Shot Exposures," *Publ. Astron. Soc. Aust*, vol. 22, no. 3, pp. 249–256, Jun. 2005, doi: 10.1071/AS05012.

[20] C. T. Kirsch, "The Cosmic Ray Background at L2 as Seen in Gaia Observations," M.S. thesis, Dr. Karl Remeis-Sternwarte Bamberg, Friedrich-Alexander-Universität Erlangen-Nürnberg, Erlangen-Nürnberg, Germany, 2018. p. 28.

[21] SATRAM dataset, "SATRAM/Timepix visualization," H. Waage and CTU Prague, Apr. 2021. [Online]. Available: https://satram.utef.cvut.cz/.

[22] D. Heynderickx, B. Quaghebeur, E. Speelman and E. Daly. (2000, Jan.). ESA's Space Environment Information System (SPENVIS) - A WWW interface to models of the space environment and its effects. *Presented at the 38th Aerosp. Sciences Meeting and Exhibit*. Reno,NV,USA. [Online]. Available: https://arc.aiaa.org/doi/10.2514/6.2000-371. Accessed: Nov. 22, 2019. doi: 10.2514/6.2000-371

[23] M. Sajid, N. G. Chechenin, F. S. Torres, E. U. Khan and S. Agha, "Space radiation environment prediction for VLSI microelectronics devices onboard a LEO satellite using OMERE-TRAD software," *Advances in Space Res.*, vol. 56, no. 2, pp. 314–324, Jul. 2015, doi: 10.1016/j.asr.2015.04.011.

[24] D. M. Sawyer and J. I. Vette, "Ap-8 trapped proton environment for solar maximum and solar minimum," *Nat. Space Sci. Data Center, Nat. Aeronaut. and Space Admin., Goddard Space Flight Center*, United States, Report N--77--18983, Dec. 1976. [Online]. Available: http://inis.iaea.org/search/search.aspx?orig_q=RN:09351076

[25] J. I. Vette, "The NASA/National Space Science Data Center: Trapped Radiation Environment Model Program (1964-1991)," *Nat. Space Sci. Data Center (NSSDC), World Data Center A for Rockets and Satellites (WDC-A-R & S), Nat. Aeronaut. and Space Admin., Goddard Space Flight Center*, United States, Technical Memorandum (TM) NASA-TM-107993; NAS 1.15:107993; NSSDC/WDC-A-R/S-91–29, Nov. 1991. [Online]. Available: https://ntrs.nasa.gov/citations/19930001815

[26] N. V. Kuznetsov, N. I. Nikolaeva, R. A. Nymmik, V. M. Uzhegov, M. V. Yakovlev and M. I. Panasyuk, "Comparison of the Models of Charged Particle Fluxes in Space," in *2015 15th Eur. Conf. on Radiat. and Its Effects on Components and Systems (RADECS)*, Moscow, Russia, Sep. 2015, pp. 178–181. doi: 10.1109/RADECS.2015.7365594.

[27] M. A. Xapsos, G. P. Summers, J. L. Barth, E. G. Stassinopoulos and E. A. Burke, "Probability model for worst case solar proton event fluences," *IEEE Trans. Nucl. Sci.*, vol. 46, no. 6, pp. 1481–1485, Dec. 1999, doi: 10.1109/23.819111.

[28] C. McCully *et al.*, *Astropy/Astroscrappy: V1.0.5 Zenodo Release*. Zenodo, 2018. doi: 10.5281/ZENODO.1482019.

[29] C. Granja and S. Polansky, "Mapping the space radiation environment in LEO orbit by the SATRAM Timepix payload on board the Proba-V satellite," *AIP Conf. Proc.*, vol. 1753, no. 1, p. 080006, Jul. 2016, doi: 10.1063/1.4955376.

[30] S. Gohl, B. Bergmann, H. Evans, P. Nieminen, A. Owens and S. Posipsil, "Study of the radiation fields in LEO with the Space Application of Timepix Radiation Monitor (SATRAM)," *Advances in Space Res.*, vol. 63, no. 5, pp. 1646–1660, Mar. 2019, doi: 10.1016/j.asr.2018.11.016.

[31] M. Paolucci *et al.*, "A real time active pixel dosimeter for interventional radiology," *Radiat. Measurements*, vol. 46, no. 11, pp. 1271–1276, Nov. 2011, doi: 10.1016/j.radmeas.2011.07.006.

[32] O. Appiah and J. B. Hayfron-Acquah, "Fast Generation of Image's Histogram Using Approximation Technique for Image Processing Algorithms," *IJIGSP*, vol. 10, no. 3, pp. 25–35, Mar. 2018, doi: 10.5815/ijigsp.2018.03.04.